Molecular Dominoes Triggered by Mechanical Stimulation and Solid Seeding as Single-Crystal-to-Single-Crystal Transformation

Hajime Ito,[*1] Mai Muromoto,[1] Sayaka Kurenuma,[1] Shoji Ishizaka,[2] Noboru Kitamura,[3] Hiroyasu Sato,[4] & Tomohiro Seki[1]

[1]Division of Chemical Process Engineering & Frontier Chemistry Center, Graduate School of Engineering, Hokkaido University, Sapporo 060-8628, Japan. Fax: +81-(0)11-706-6561, email: hajito@eng.hokudai.ac.jp

[2]Department of Chemistry, Graduate School of Science, Hiroshima University, Higashi-Hiroshima 739-8526, Japan. Fax: +81-(0)82-424-7425

[3]Department of Chemistry, Faculty of Science, Hokkaido University, Sapporo, Hokkaido, 060-0810, Japan. Fax: +81-(0)11-706-2697

[4]Rigaku Corporation, Akishima, Tokyo 196-8666, Japan. Fax: +81-(0)546-8158

Abstract

Numerous studies have focused on the mechanical control of solid structures and phase changes in molecular crystals. However, the molecular level understanding of how macroscopic forces affect the molecules in a solid remains incomplete. Here, we report that a small mechanical stimulus or solid seeding can trigger a single-crystal-to-single-crystal transformation from a kinetically isolated polymorph of phenyl(phenyl isocyanide)gold(I) exhibiting blue photoluminescence to a thermodynamically stable polymorph exhibiting yellow emission without the need for heating or solvent. The phase transformation initiates at the location of the mechanical stimulation or seed crystal, extends to adjacent crystals, and can be readily monitored visually by the accompanying photoluminescent color change from blue to yellow. The transformation was characterized using single crystal X-ray analysis. Our results suggest that the transformation proceeds through self-replication, causing the complex to behave as ‘molecular dominoes’.

Introduction

Single-crystal-to-single-crystal (SCSC) transformations in molecular crystals are known to be induced by various external perturbations, such as heat, light, static pressure and exposure to small molecules.[1–11] The crystal structures can be compared before and after the structure change using single crystal X-ray diffraction (XRD) analysis, providing a molecular level understanding of the solid state reactions and phase transformations.[12,13] Anisotropic addition of a bulk force, such as shearing, ball-milling or grinding, can also alter the solid structure of the molecular crystals, and numerous studies have suggested that this transformation can include direct crystal-to-crystal conversion.[14–21] However, anisotropic forces also induce crystal collapse, making them unsuitable for single crystal X-ray analysis. To date, the observation of a SCSC transformation induced by a mechanical stimulus has not yet been reported.

In this paper, we report the first observation of the SCSC transformation of phenyl(phenyl isocyanide)gold(I) (**1**), which was triggered by applying a small mechanical force to the crystal surface or by contact with a crystal seed of the opposite polymorph. The phase change first occurred at the initial contact area and subsequently progressed spontaneously throughout the entire crystal. Single crystal X-ray analysis was performed on the resulting crystals, providing molecular level information on the phase transformation. Distinctive structural changes were observed, including a transition from

CH/π to aurophilic intermolecular interactions.[23–25] The phase change was accompanied by a drastic luminescence color change caused by the switching of the intermolecular interactions. This color change allowed the progression of the phase change to be clearly visualized.

Results

Synthesis of 1 and its polymorph $\mathbf{I_b}$. During the course of our studies on the luminescence mechanochromism of gold(I) complexes,[14] we synthesized **1** in high yield (89%) through the reaction of chloro(phenyl isocyanide)gold(I) with phenyllithium for 1 h at –78 °C (Figure 1a). Careful but rapid crystallization from a hexane/dichloromethane solution produced crystals of **1** in the $\mathbf{I_b}$ phase. Blue photoluminescence was observed from $\mathbf{I_b}$ crystals under UV irradiation with emission maxima at 460 and 490 nm [quantum yield $\Phi^{em} = 0.15$, lifetime: $\tau_1 = 1.47$ μs ($A_1 = 0.92$), $\tau_2 = 72.1$ μs ($A_1 = 0.08$), $\lambda_{ex} = 355$ nm] (Figure 1b, blue solid line; Figure 2a). The excitation spectrum of $\mathbf{I_b}$ displayed a peak at 315 nm (Figure 1b, blue dotted line). The crystal structure of $\mathbf{I_b}$ was determined by the XRD of a single crystal (Figure 2a–d; Supplementary Figure S1; Supplementary Tables S1 and 2). $\mathbf{I_b}$ was found to be triclinic (*P-1*, $a = 6.0214(5)$ Å, $b = 9.0729(8)$ Å, $c = 11.4498(10)$ Å, $\alpha = 102.159(7)°$, $\beta = 101.468(7)°$, $\gamma = 102.358(7)°$ at 123 K, $Z = 2$, $R_1 = 3.3\%$, ${}_wR_2 = 8.2\%$, GOF = 1.056, calculated density: 2.169 g/cm^3). X-ray analysis, elemental analysis, thermal gravimetric analysis (TGA) and ^{1}H NMR measurements of $\mathbf{I_b}$ indicated that there was no solvent inclusion in the crystals

(Supplementary Figures S2 and S3; Supplementary Table S3; Supplementary Notes S1). Each of the molecules in $\mathbf{I_b}$ formed a herringbone-like structure with a head-to-tail arrangement of the phenyl ligand on the gold atoms, and the isocyanide phenyl moiety twisted with a dihedral angle of 71.6º (Figure 2b).[22] There were large distances (> 4.65 Å) between the gold atoms of adjacent molecules, indicating the absence of aurophilic interactions, which typically possess Au···Au distances of less than 3.5 Å in solid-state structures.[23,24] Time-dependent density functional theory (TDDFT) calculations were performed based on the crystal structure of $\mathbf{I_b}$, affording insight into its excitation by metal-perturbed ligand-to-ligand charge transfer (LLCT) (Supplementary Figures S4–8; Supplementary Tables S4–S6).

Solution-phase preparation of polymorph $\mathbf{II_y}$. The slow crystallization of **1** from a hexane/dichloromethane solution produced the polymorphic crystals $\mathbf{II_y}$, which exhibited a significantly different crystal structure compared with that of $\mathbf{I_b}$. The $\mathbf{II_y}$ crystals exhibited a strong yellow emission (λ_{max} = 571 nm) under UV irradiation (365 nm) (Figure 1b, red solid line and Figure 2e). A higher emission quantum yield [Φ^{em} = 0.43] and shorter emission lifetime [τ_1 = 0.17 μs (A_1 = 0.20), τ_2 = 0.65 μs (A_2 = 0.80), λ_{ex} = 355 nm] were observed compared with those for $\mathbf{I_b}$. The excitation spectrum of $\mathbf{II_y}$ displayed a peak at a longer wavelength (432 nm) than that of $\mathbf{I_b}$ (Figure 1b, red dotted line). The crystal structure of $\mathbf{II_y}$ was in the tetragonal system with a space group of

I-42d (Figure 2f–h, a = 13.4781(4) Å, c = 24.8079(8) Å at 123 K, Z = 16, R_1 = 2.5%, $_wR_2$ = 5.4%, GOF = 1.093, calculated density: 2.224 g/cm^3, Supplementary Figure S9; Supplementary Tables S1 and S2). X-ray analysis, elemental analysis and ^{1}H NMR measurements of **II$_y$** indicated that there was no solvent inclusion in the crystals (Supplementary Figure S2; Supplementary Table S3; Supplementary Note 1). The molecules of **II$_y$** adopted a nearly flat conformation with a dihedral angle between the isocyanide phenyl group and the gold-coordinated phenyl group of 3.1º. Oblique head-to-tail dimers contained a short Au···Au distance of 3.177 Å, suggesting the presence of significant aurophilic interactions.[23,24] Each dimer interacted with adjacent dimers through isocyanide carbons separated by just 3.186 Å to form 1-D chain-like structures comprising dimer units (Supplementary Figure S9). TDDFT calculations of a model structure based on the **II$_y$** crystals indicated a metal–metal to ligand charge transfer characteristic that was facilitated by the short Au···Au distance (Supplementary Figures S4, S10, S11; Supplementary Tables S4 and S7).[23,24]

Luminescent mechanochromism of I$_b$. The blue luminescent **I$_b$** displayed a significant luminescence mechanochromism (Figure 3a).[14–17] The ball-milling of **I$_b$** for 3 min afforded the powder **II$_{y(\text{ground Ib})}$**, which was identical to crystalline **II$_y$** in terms of its photoluminescence and solid state structure. Similar to **II$_y$**, **II$_{y(\text{ground Ib})}$** exhibited a luminescence maximum at 567 nm, an emission quantum yield of 0.38, and emission lifetimes of τ_1 = 0.27 μs (A_1 = 0.34) and τ_2 = 0.68 μs (A_1 =

0.66) at an excitation wavelength of 355 nm (Figure 2b, black solid line) with an excitation peak at 400 nm (Figure 2b, black dotted line). The powder XRD pattern of the ball-milled sample (**II**$_{\mathbf{y(ground\ Ib)}}$, Figure 1c, black solid line) matched the simulated diffraction pattern based on the single crystal X-ray analysis of **II**$_{\mathbf{y}}$ (Figure 1c, red solid line), and no trace of **I**$_{\mathbf{b}}$ was found in the ball-milled sample (Figure 1c, blue solid line). These results indicate that the ball-milling process induced direct crystal-to-crystal transformation of **I**$_{\mathbf{b}}$ to **II**$_{\mathbf{y}}$.

SCSC transformation. The ball-milling described above involves a considerable mechanical stimulus; we next conducted the mechanical triggering experiment with a much smaller stimulus. A small pit was formed on the surface of an **I**$_{\mathbf{b}}$ crystal using a needle under atmospheric conditions (Figure 3b). A yellow luminescent spot was initially observed at the location of the small pit. Subsequently, the domain exhibiting yellow emission gradually increased to nearly the entire crystal after 9 h at room temperature. The transformation could also be triggered by contacting a seed crystal of **II**$_{\mathbf{y}}$ with a crystal of **I**$_{\mathbf{b}}$ (Figure 3c). The luminescent color change initiated at the point of contact and extended to the entire crystal after 15 h. This color change propagated through the contacting surfaces of adjacent crystals; eventually, the blue luminescent crystals that were in contact with neighboring yellow luminescent crystals became yellow, maintaining their transparency (Figure 3d and e, Supplementary Figure 12). This solid-seeding phase change represents a self-replicating

progression of phase transformation. It should be noted that the rate of conversion was highly variable: some crystals changed rapidly, whereas others were slower.

Single crystal X-ray analysis was performed after the mechanical stimulus-triggered SCSC transformation of $\mathbf{I_b}$. A yellow luminescent crystal was prepared by the mechanical pricking of a small region of one $\mathbf{I_b}$ crystal. After the initial contact area was removed to avoid affecting the quality of the XRD data, the yellow emissive crystal (denoted $\mathbf{II_{yscsc}}$) was subjected to single crystal X-ray analysis. The crystal structure of $\mathbf{II_{yscsc}}$ obtained *via* SCSC was identical to that of $\mathbf{II_y}$ crystallized from the solution phase (Figure 3f; Supplementary Figure S13; Supplementary Tables S1 and S2; $\mathbf{II_{yscsc}}$: a = 13.4075(19) Å, c = 24.9673(19) Å at 123 K, Z = 16, R_1 = 8.8%, ${}_wR_2$ = 21.7%, GOF = 1.316, calculated density: 2.233 g/cm^3).

Discussion.

The mechanical- or solid seeding-triggered phase change described in this study occurred at room temperature, whereas a thermal phase transformation of $\mathbf{I_b}$ to $\mathbf{II_y}$ required elevated temperatures of 64.5–74.9 °C (Supplementary Figure S3). No reverse phase change was observed when the sample was cooled. The $\mathbf{I_b}$ crystal could only be regenerated by the dissolution and recrystallization of $\mathbf{II_y}$.

The thermal analysis suggested that $\mathbf{I_b}$ was a metastable, kinetically isolated form of **1**, and $\mathbf{II_y}$ was the thermodynamically favored form (Supplementary Figure S14). The thermodynamic analysis and the sample crystallization process revealed that **1** is a good example of the Ostwald rule: the less stable polymorphs ($\mathbf{I_b}$) crystallize first, and the more stable polymorphs ($\mathbf{II_y}$) form later.[1–3] In some reports, mechanical pricking or the presence of defects can accelerate the phase change near the thermal phase change temperature, resulting in polycrystalline formation.[1,3,13,25] However, the phase transformation of $\mathbf{I_b}$ occurred at much lower temperatures, suggesting that the transformation observed in our study was triggered purely by mechanical stimulation. To our knowledge, this is the first clear example of the mechanical- or solid seeding-trigged SCSC transformation of molecular crystals. In addition, the emergence of metallophilic interactions after the SCSC transformation of mother crystals lacking metallophilic interactions has not been reported previously.

The solid-state structures of $\mathbf{I_b}$ and $\mathbf{II_y}$ varied greatly (triclinic *P-1* and tetragonal *I-42d*) (See Supplementary Figure S15). Thus, the significant structural transformation cannot be explained by a simple conformational change or molecular reorientation. The phase change may proceed by a similar mechanism to the epitaxial mechanism proposed for the thermal phase transformation.[3,25] A small portion of the $\mathbf{II_y}$ daughter phase forms initially in the $\mathbf{I_b}$ mother phase through mechanical stress or contact with a seed crystal of $\mathbf{II_y}$ (Figure 4a and b). The molecules in the thermodynamically

unstable $\mathbf{I_b}$ phase diffuse across the narrow gap between phases $\mathbf{I_b}$ and $\mathbf{II_y}$ and rearrange to the $\mathbf{II_y}$ phase through the formation of intermolecular aurophilic interactions (Figure 4c and d)

This phase transformation resembles dominoes, in that a mechanical stimulus (pushing) triggers a state change in the entire assembly. The self-replicative nature of this molecular domino may provide a new way to control nano or molecular structures through macroscopic mechanical stimulation. The domino-like amplification of the optical response to the small mechanical stimulus (from the small pit to the entire crystal) can be applied to the highly sensitive detection of mechanical stimulation.

Methods

Synthesis of 1. Chloro(phenyl isocyanide)gold(I) was prepared from chloro(tetrahydrothiophene)gold(I) and phenyl isocyanide using a method similar to that reported previously.[26] Chloro(phenyl isocyanide)gold(I) (100.7 mg, 0.30 mmol) and a magnetic stir bar were placed in a vial and sealed with a rubber septum. After the reaction vial was connected to a vacuum manifold through a needle, it was evacuated and then back filled with nitrogen. Dry THF (0.44 mL) was added *via* a syringe to dissolve the chloro(phenyl isocyanide)gold(I). A butyl ether solution of phenyllithium (0.164 mL, 1.83 M, 0.30 mmol) was added at –78 ºC under stirring. After 30 min, the reaction was quenched by the addition of a saturated aqueous solution of NH_4Cl (2 mL), extracted three times with CH_2Cl_2, washed with brine and then dried over $MgSO_4$. After filtration, the volatiles were removed under reduced pressure. Crude phenyl(phenyl isocyanide)gold(I) (**1**) was obtained as a pale purple solid (106.7 mg, 89%). The yield was determined by ^1H NMR spectroscopy using $Cl_2CHCHCl_2$ as an internal standard. **1** was recrystallized from CH_2Cl_2/hexane after filtration to remove an insoluble purple solid. **1** was fairly stable in air at room temperature, but readily decomposed at elevated temperatures (>80 °C), with metal deposition occurring on its surface. In solution, **1** remained intact in the dark for a short period (< 1 h) but readily decomposed under light. The data for ^1H and ^{13}C NMR and HRMS were included as Supplementary Information.

Crystal and Powder Sample Preparation ($\mathbf{I_b}$, $\mathbf{II_y}$). Typical preparation procedures are as follows. On the surface of a solution of **1** (prepared from $\mathbf{I_b}$ or $\mathbf{II_y}$, 20 mg) in CH_2Cl_2 (1.0 mL)/hexane (2.0 mL) in a small glass vial, a stream of nitrogen gas was flowed through a needle connected to a nitrogen line for a few minutes to produce crystals of $\mathbf{I_b}$. $\mathbf{II_y}$ crystals were obtained by the slow crystallization (typically 10 h) of a solution of **1** in CH_2Cl_2/hexane placed in a refrigerator. The ground sample of $\mathbf{II_{y(ground\ Ib)}}$ was prepared with a ball mill (Taitec Bead Crusher μT-01, Koshigaya, Saitama, Japan). Typically, $\mathbf{I_b}$ (50 mg) was treated in a micro tube (ϕ13 × 49 mm) with a screw cap at a shaking speed of 4600 r/min for 3 min (60 s three times) using a stainless bead (1/8 inch).

Single Crystal and Powder X-ray Analysis. Measurements for $\mathbf{I_b}$, $\mathbf{II_y}$, and $\mathbf{II_{yscsc}}$ were made on a Rigaku R-AXIS RAPID diffractometer using graphite monochromatic Mo-K_α radiation. The diffraction data were collected at –150 °C. The structure was solved by direct methods and expanded using Fourier techniques. Non-hydrogen atoms were refined anisotropically. Hydrogen atoms were refined using the riding model. All calculations were performed using the CrystalStructure crystallographic software package, except for refinement, which was performed using SHELXL-97. The powder diffraction data for $\mathbf{II_{y(ground\ Ib)}}$ were recorded at room temperature on a Rigaku SmartLab diffractometer with Cu-K_α radiation and a D/teX Ultra detector covering 5–50° (2θ). The diffraction data were collected at 20 °C. The powder simulation patterns for $\mathbf{I_b}$ and $\mathbf{II_y}$ were

generated from the single crystal X-ray structures collected at 20 °C. The powder patterns for $\mathbf{I_b}$ and $\mathbf{II_y}$ displayed in Figure 1b were generated using Mercury 3.0.

References

1 Bernstein, J. *Polymorphism in molecular crystals*. (Oxford University Press, 2002).

2 Wildfong, P. L. D. *Polymorphism in pharmaceutical solids*. 2nd edn, (Informa Healthcare, 2009).

3 Mnyukh, Y. *Fundamentals of solid-state phase transitions, ferromagnetism and ferroelectricity, 2nd edition*. (Direct Scientific Press, 2010).

4 Kobatake, S., Takami, S., Muto, H., Ishikawa, T. & Irie, M. Rapid and reversible shape changes of molecular crystals on photoirradiation. *Nature* **446**, 778–781 (2007).

5 Mutai, T., Satou, H. & Araki, K. Reproducible on-off switching of solid-state luminescence by controlling molecular packing through heat-mode interconversion. *Nat. Mater.* **4**, 685–687 (2005).

6 Huang, Z., White, P. S. & Brookhart, M. Ligand exchanges and selective catalytic hydrogenation in molecular single crystals. *Nature* **465**, 598–601 (2010).

7 Malwitz, M. A. *et al.* Crystallization and Interconversions of Vapor-Sensitive, Luminescent Polymorphs of $[(C_6H_{11}NC)_2AuI](AsF_6)$ and $[(C_6H_{11}NC)_2AuI](PF_6)$. *J. Am. Chem. Soc.* **134**, 10885–10893 (2012).

8 Zenkina, O. V., Keske, E. C., Wang, R. & Crudden, C. M. Double

single-crystal-to-single-crystal transformation and small-molecule activation in rhodium nhc complexes. *Angew. Chem., Int. Edit.* **50**, 8100–8104 (2011).

9 Biradha, K. & Fujita, M. A springlike 3D-coordination network that shrinks or swells in a crystal-to-crystal manner upon guest removal or readsorption. *Angew. Chem., Int. Edit.* **41**, 3392–3395 (2002).

10 Wu, C.-D. & Lin, W. Highly porous, homochiral metal-organic frameworks: solvent-exchange-induced single-crystal to single-crystal transformations. *Angew. Chem., Int. Edit.* **44**, 1958–1961 (2005).

11 Albrecht, M., Lutz, M., Spek, A. & van Koten, G. Organoplatinum crystals for gas-triggered switches. *Nature* **406**, 970–974 (2000).

12 Halasz, I. Single-crystal-to-single-crystal reactivity: gray, rather than black or white. *Cryst. Growth Des.* **10**, 2817-2823 (2010).

13 Desiraju, G. R., Vittal, J. J. & Ramanan, A. *Crystal engineering : a textbook*. (World Scientific ; IISc Press, 2011).

14 Ito, H. *et al.* Reversible mechanochromic luminescence of [$(C_6F_5Au)_2$(μ-1,4-diisocyanobenzene)]. *J. Am. Chem. Soc.* **130**, 10044–10045 (2008).

15 Sagara, Y. & Kato, T. Mechanically induced luminescence changes in molecular assemblies.

Nat. Chem. **1**, 605–610 (2009).

16 Ariga, K., Mori, T. & Hill, J. P. Mechanical control of nanomaterials and nanosystems. *Adv. Mater.* **24**, 158–176 (2012).

17 Balch, A. Dynamic crystals: visually detected mechanochemical changes in the luminescence of gold and other transition-metal complexes. *Angew. Chem., Int. Edit.* **48**, 2641–2644 (2009).

18 Descamps, M., Willart, J. F., Dudognon, E. & Caron, V. Transformation of pharmaceutical compounds upon milling and comilling: The role of Tg. *J. Pharm. Sci.* **96**, 1398–1407 (2007).

19 Brittain, H. G. Effects of mechanical processing on phase composition. *J. Pharm. Sci.* **91**, 1573–1580 (2002).

20 Wildfong, P. L. D., Morris, K. R., Anderson, C. A. & Short, S. M. Demonstration of a shear-based solid-state phase transformation in a small molecular organic system: Chlorpropamide. *J. Pharm. Sci.* **96**, 1100–1113 (2007).

21 Braga, D., Grepioni, F. & Maini, L. The growing world of crystal forms. *Chem. Commun.* **46**, 6232–6242 (2010).

22 Tiekink, E. R. T. & Zukerman-Schpector, J. *The importance of Pi-interactions in crystal*

engineering : frontiers in crystal engineering. (Wiley, 2012).

23 Schmidbaur, H. & Schier, A. A briefing on aurophilicity. *Chem. Soc. Rev.* **37**, 1931–1951 (2008).

24 Yam, V. W.-W. & Cheng, E. C.-C. Highlights on the recent advances in gold chemistry – a photophysical perspective. *Chem. Soc. Rev.* **37**, 1806–1813 (2008).

25 Herbstein, F. H. On the mechanism of some first-order enantiotropic solid-state phase transitions: from Simon through Ubbelohde to Mnyukh. *Acta Crystallogr., Sect. B: Struct. Sci.* **62**, 341–383 (2006).

26. Hashmi, A. S. K., Yu, Y. & Rominger, F. Efficient One-Pot Synthesis of Unsymmetrical Gold(I) *N*-Heterocyclic Carbene Complexes and Their Use as Catalysts. *Organometallics* **31**, 895–904 (2012).

Accession codes: The X-ray crystallographic coordinates for the structures reported in this article have been deposited at the Cambridge Crystallographic Data Centre (CCDC) under deposition number CCDC 897541, 897542, and 909344. These data can be obtained free of charge from The Cambridge Crystallographic Data Centre via www.ccdc.cam.ac.uk/data_request/cif.

Supplementary Information is linked to the online version of the paper at www.nature.com/nature.

Acknowledgements: The Funding Program for Next Generation World-Leading Researchers (NEXT Program, No. GR002) is gratefully acknowledged. We thank Professor Masaya Sawamura and Professor Yoshihide Nakao for their suggestions. We appreciate Professor Toyoji Kakuchi, Professor Toshihumi Sato and Kenta Sakurada for thier help with TGA analysis.

Author contributions H. I. wrote this paper. S. I., N. K., and T. S. helped with the spectroscopic analysis. S. H. did the XRD measurements and analyses. M. M. and S. K. synthesized **1** and performed all the other experiments.

Author information The authors declare no competing financial interests. Readers are welcome to comment on the online version of this article at www.nature.com/nature. Correspondence and requests for materials should be addressed to H. I. (hajito@eng.hokudai.ac.jp).

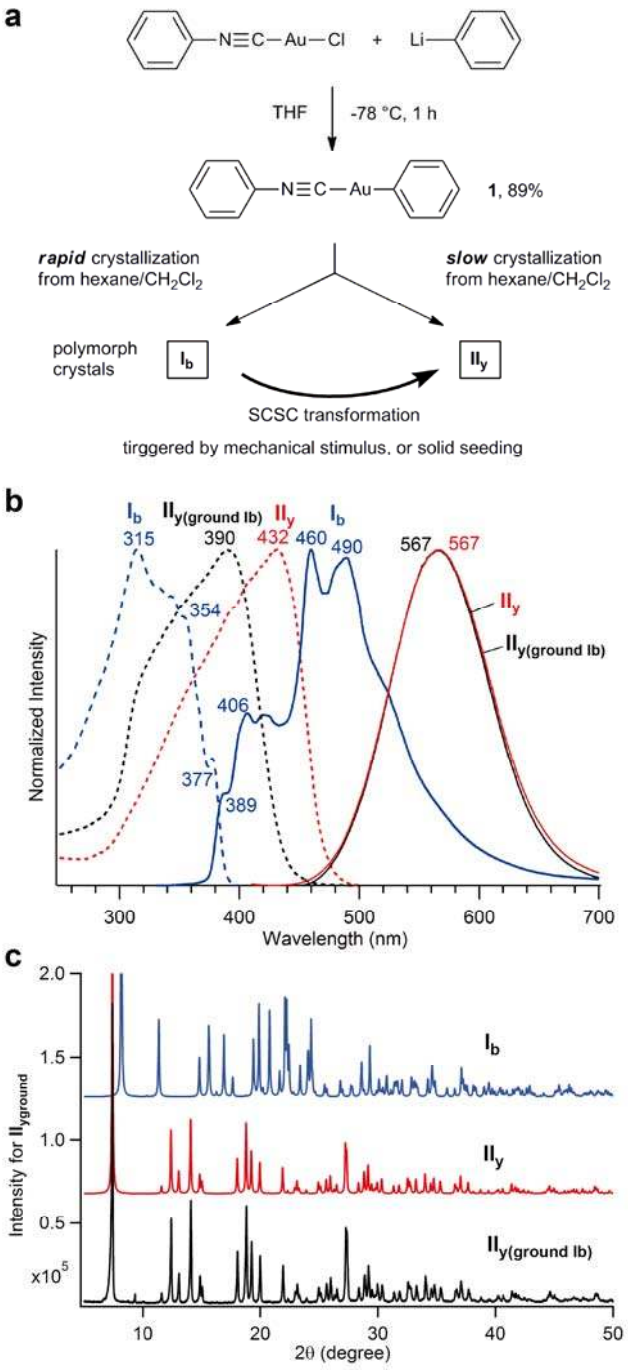

Figure 1 Structure, Optical Properties, and Phase Transformations of 1. a, Synthesis, crystallization and phase conversions of **1**. **b**, Emission and excitation spectra, displayed as solid and dotted lines, respectively. Blue: $\mathbf{I_b}$ (excited at 315 nm for the emission spectrum, observed at 460 nm

for the excitation spectrum), red: $\mathbf{II_y}$ (excited at 432 nm, observed at 565 nm), black: $\mathbf{II_{y(ground\ Ib)}}$ (excited at 385 nm, observed at 565 nm). **c**, Powder diffraction of $\mathbf{II_{y(ground\ Ib)}}$ (black line) and simulated diffraction patterns for $\mathbf{II_y}$ (red line) and $\mathbf{I_b}$ (blue line).

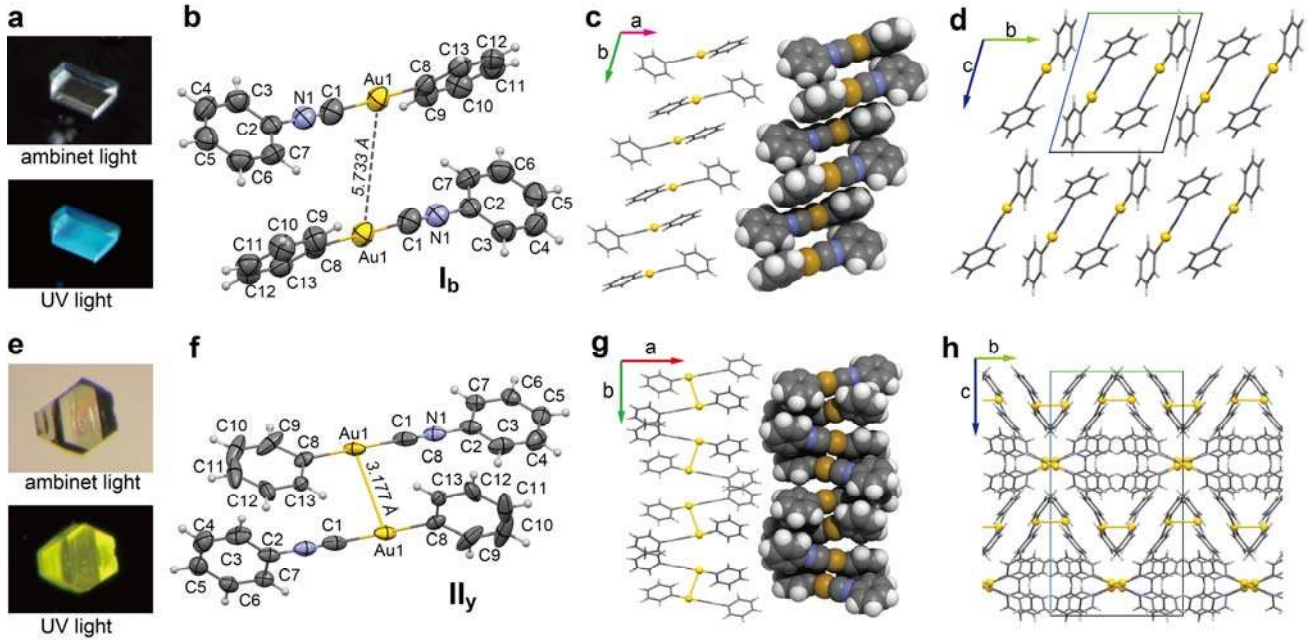

Figure 2 Photographs and Crystal Structures of Polymorphs $\mathbf{I_b}$ and $\mathbf{II_y}$. **a**, Photographs of polymorph $\mathbf{I_b}$ under ambient and ultraviolet (UV, 365 nm) light. **b**, Oak Ridge Thermal Ellipsoid Program (ORTEP) drawing (50% probability level) of the crystal structure of $\mathbf{I_b}$. **c**, Crystal structure of $\mathbf{I_b}$ depicted as stick and space filling models viewed along the *c* axis. **d**, Crystal structure of $\mathbf{I_b}$ viewed along the *a* axis. **e**, Photographs of the polymorph $\mathbf{II_y}$ under ambient and UV (365 nm) light. **f**, ORTEP drawing (50% probability level) of the crystal structure of $\mathbf{II_y}$. **g** and **h**, Crystal structures

of $\mathbf{II_y}$.

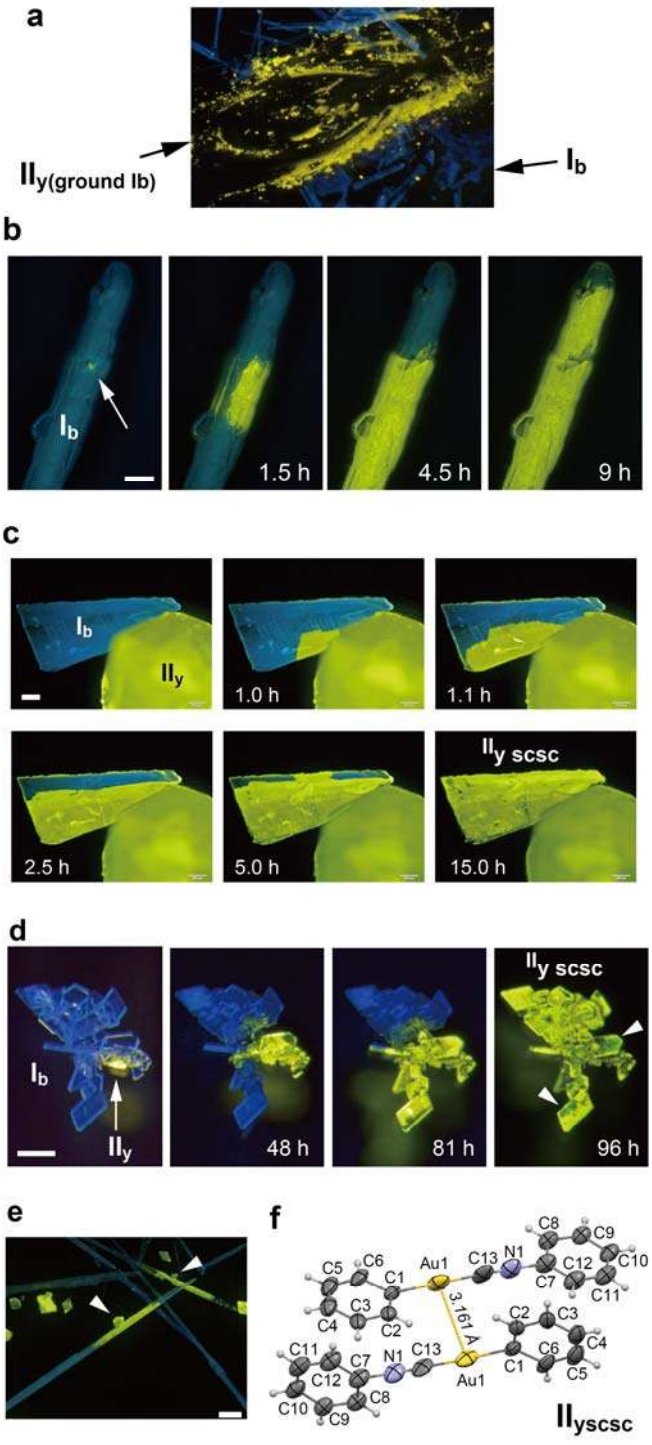

Figure 3 Photographs of the phase transformation of $\mathbf{I_b}$ to $\mathbf{II_y}$. **a**, Luminescence mechanochromism of $\mathbf{I_b}$. Yellow luminescent $\mathbf{II_{y(ground\ Ib)}}$ was generated by grinding the blue luminescent $\mathbf{I_b}$ powder with a spatula**. b**, Mechanical stimulus-triggered phase transformation (scale bar 200 μm). A small pit (left, white arrow) was first produced by pricking the fixed sample with a needle. The phase transformation gradually spread over the entire crystal after 9 h. **c**, Solid seeding-triggered phase transformation (scale bar 200 μm). The phase transformation of $\mathbf{I_b}$ initiated from the area in contact with the seed crystal of $\mathbf{II_y}$ (upper left photograph) and spread over the entire crystal after 15 h (lower right photograph). **d**, Progression of the phase transformation over the crystals (scale bar 200 μm). Partial decomposition of the $\mathbf{II_y}$ phase was observed (white triangles). **e**, Progression of phase transformation from the seed crystals (white triangles, scale bar 200 μm). **f**, Crystal structure of $\mathbf{II_{yscsc}}$. These mechanical- and seeding-triggered phase transformation experiments could be replicated many times; however, the conversion rate varied considerably from crystal to crystal.

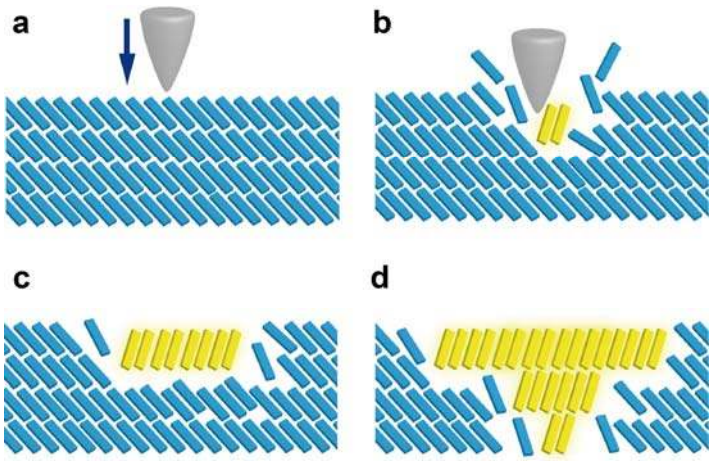

Figure 4 Proposed mechanism for the mechanical stimulus-triggered phase transformation. a, Mechanical stimulation of the metastable $\mathbf{I_b}$ phase (blue rectangles). **b**, Generation of the $\mathbf{II_y}$ phase. **c** and **d**, The thermodynamically stable $\mathbf{II_y}$ phase extends by absorbing molecules from the metastable $\mathbf{I_b}$ phase.

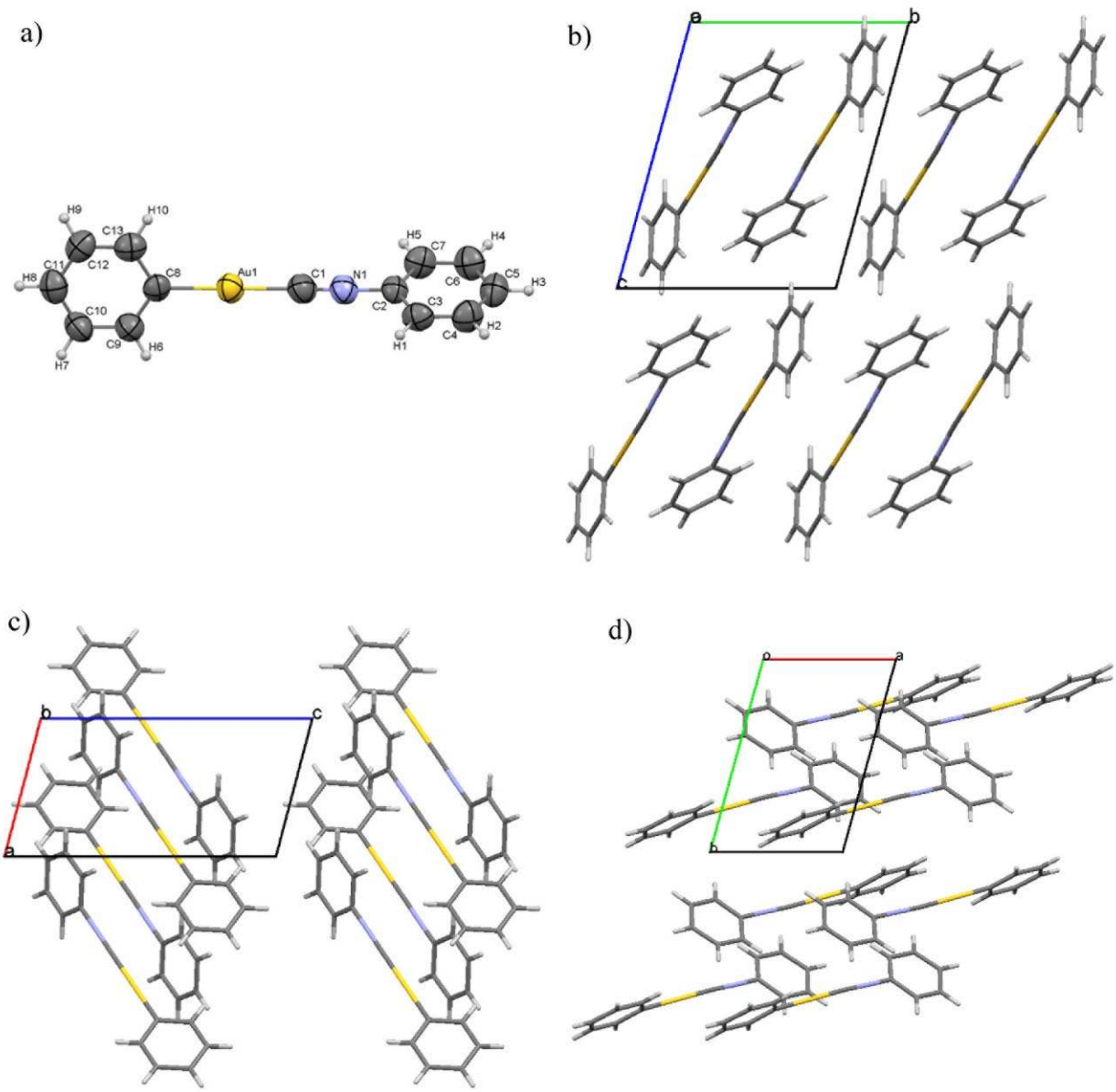

Supplementary Figure S1. X-ray crystallographic analysis of $\mathbf{I_b}$ (CCDC 909344). a) ORTEP structure. b) Molecular packing viewed along the *a* axis. c) Molecular packing viewed along the *b* axis. d) Molecular packing viewed along the *c* axis.

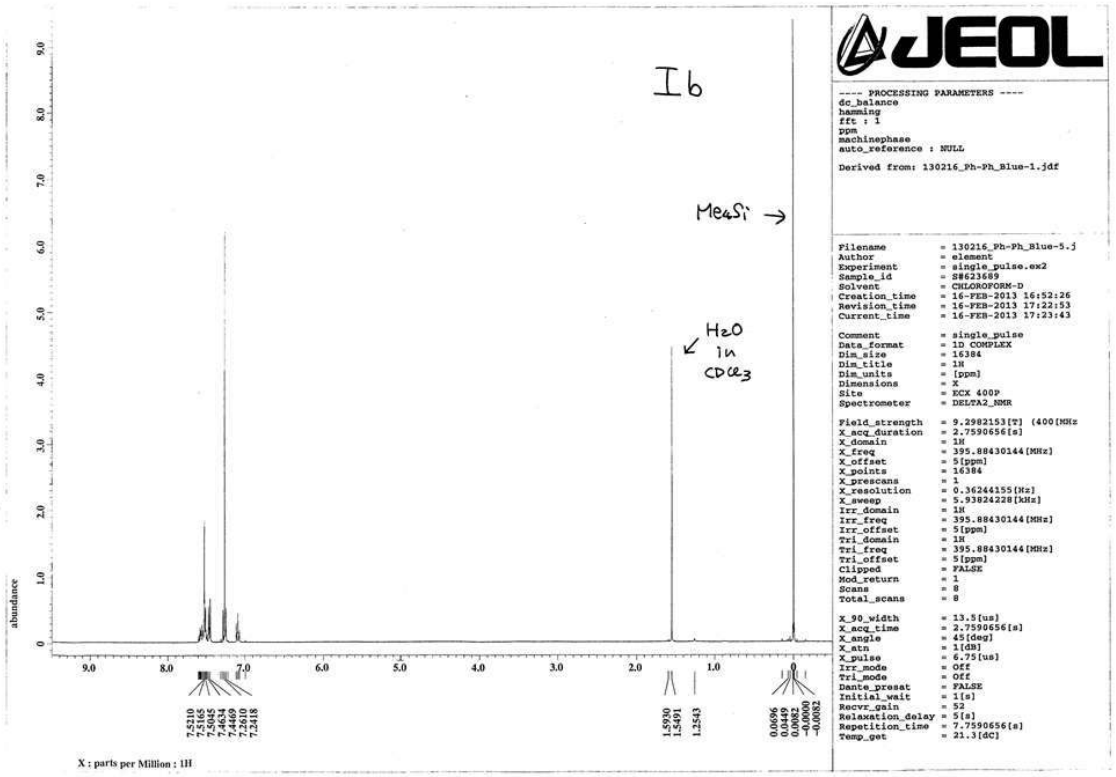

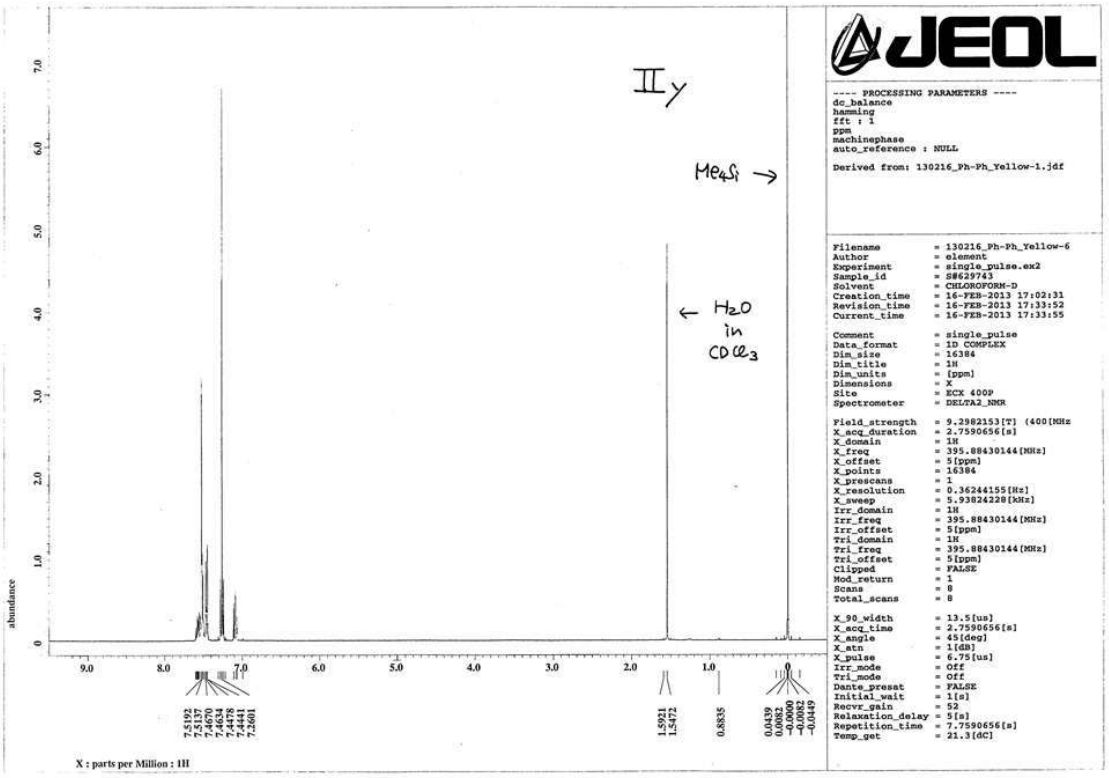

Supplementary Figure S2. ^{1}H NMR measurements of $\mathbf{I_b}$ and $\mathbf{II_y}$ crystals.

a)

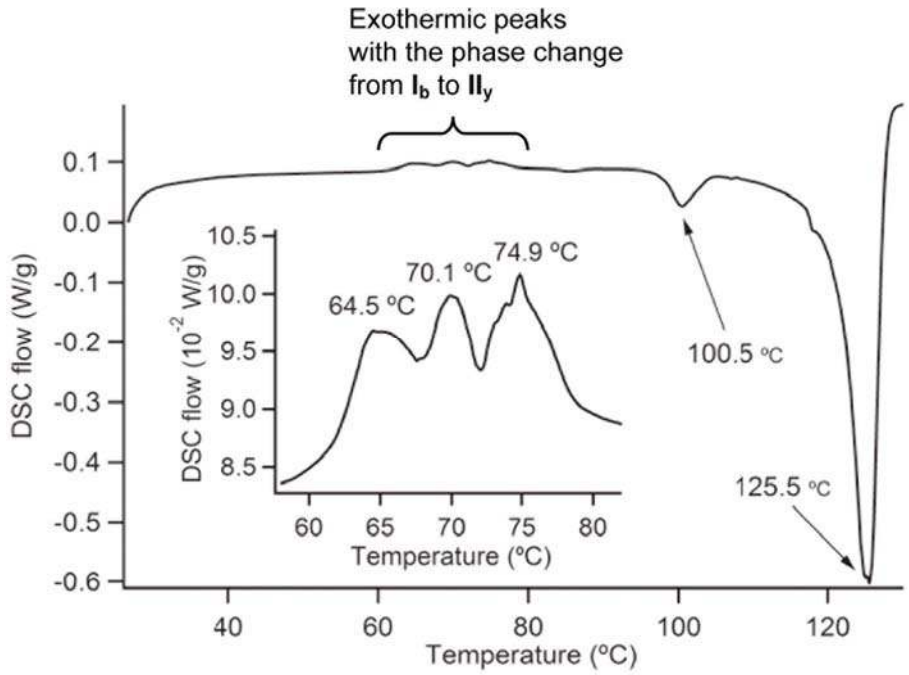

b)

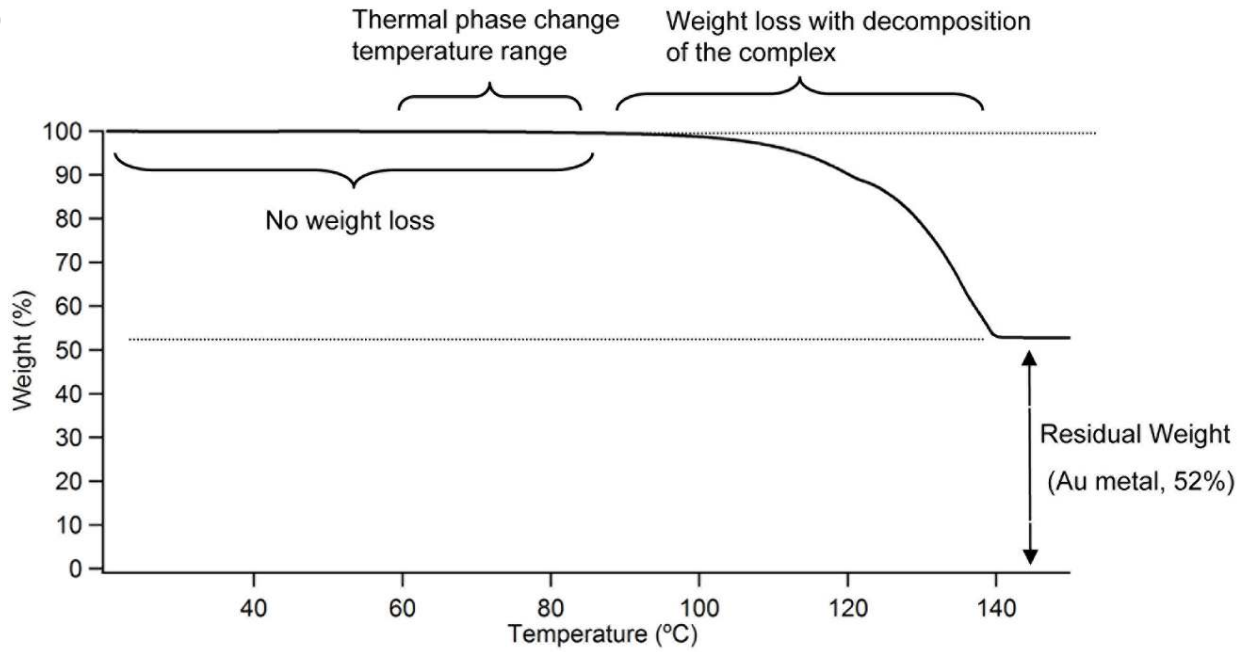

Supplementary Figure S3. Thermal Analyses. a) DSC analysis of $\mathbf{I_b}$ crystals at a heating rate of 10 °C/min. b) TGA analysis of $\mathbf{I_b}$ crystals at a heating rate of 5 °C/min.

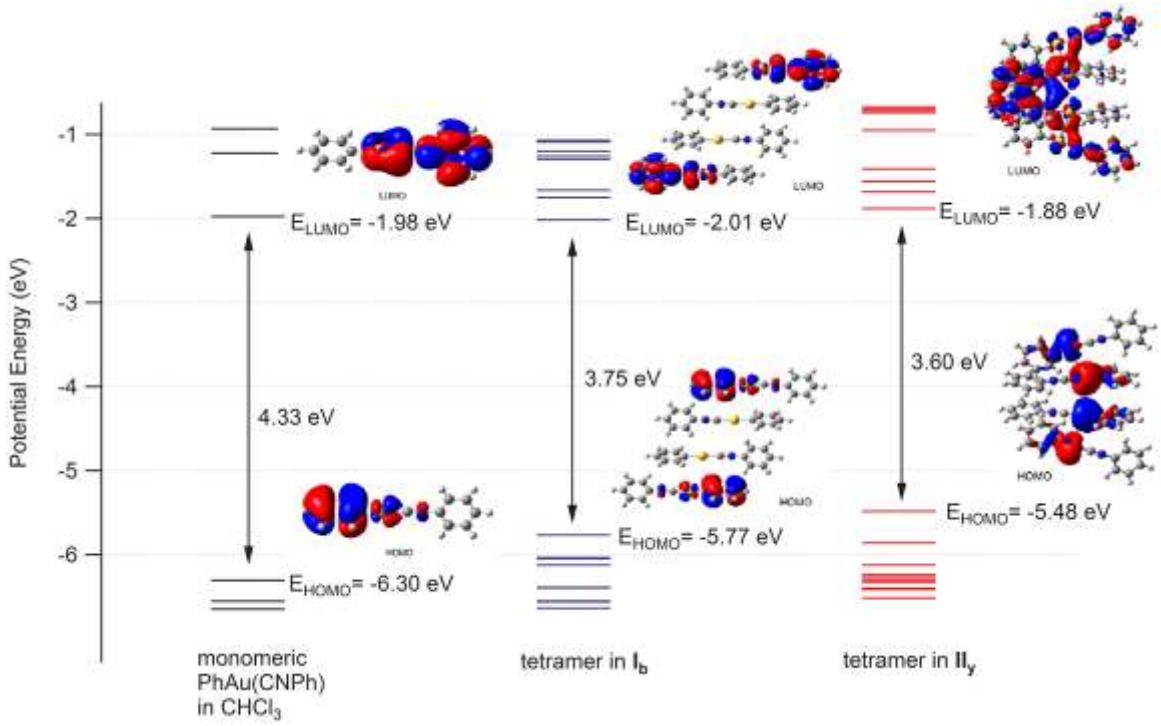

Supplementary Figure S4. Potential energies of the molecular orbitals of monomeric **1** (in $CHCl_3$), and tetrameric model structures of $\mathbf{I_b}$ and $\mathbf{II_y}$.

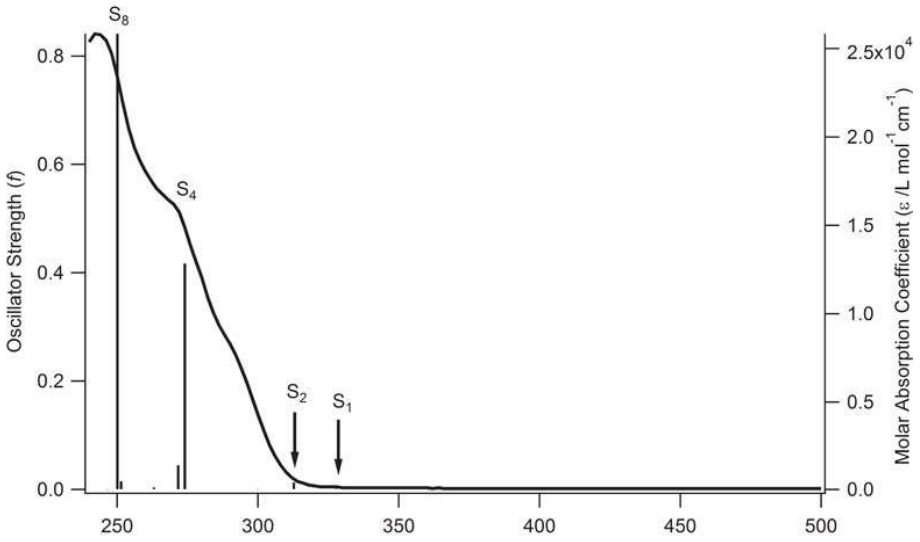

Supplementary Figure S5. Absorption spectrum of **1** in $CHCl_3$. Transitions calculated using B3LYP are overlaid.

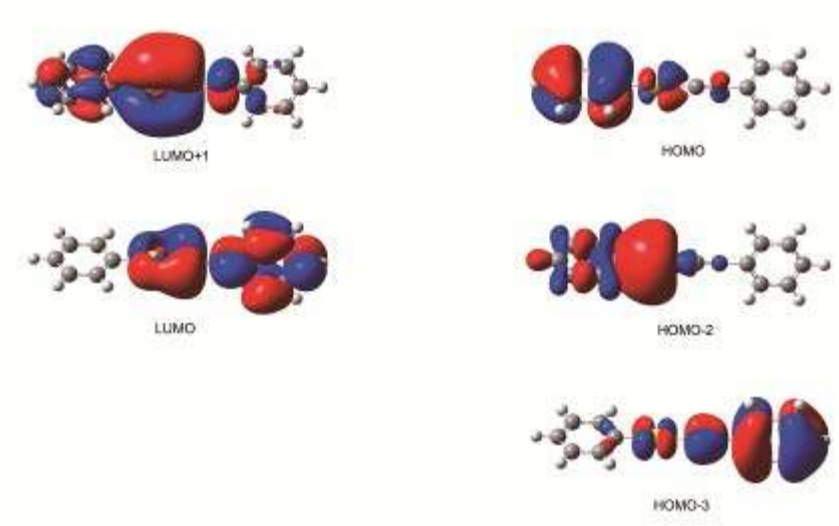

Supplementary Figure S6. Molecular orbitals of a model structure of **1** in $CHCl_3$ solution.

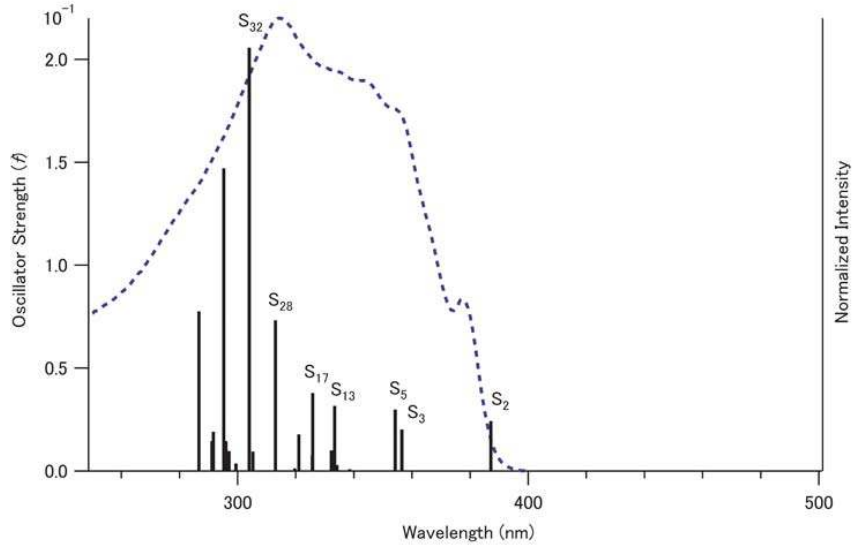

Supplementary Figure S7. Excitation spectrum of $\mathbf{I_b}$. Transitions calculated using B3LYP are overlaid.

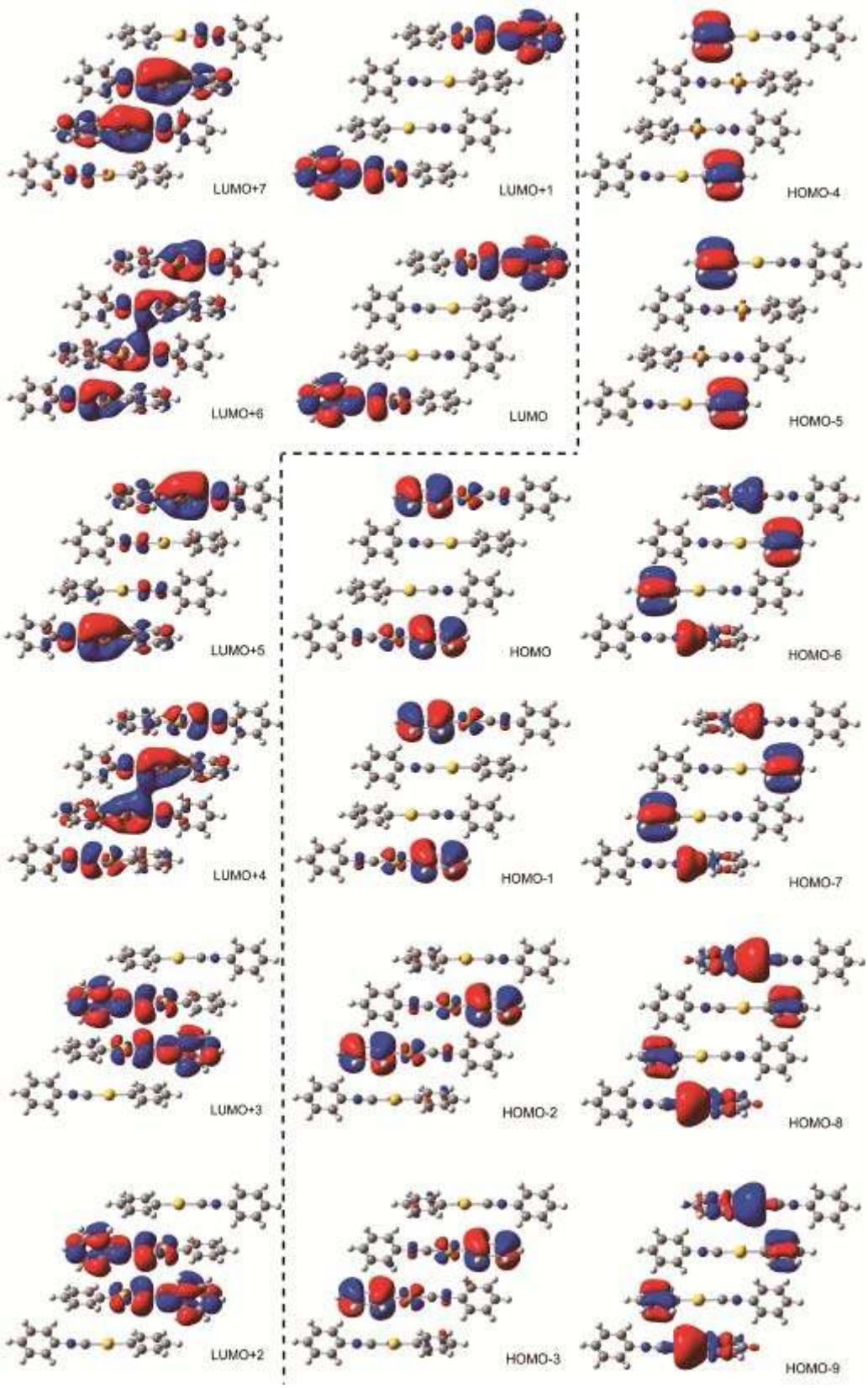

Supplementary Figure S8. Molecular orbitals of a model tetrameric structure of $\mathbf{I_b}$.

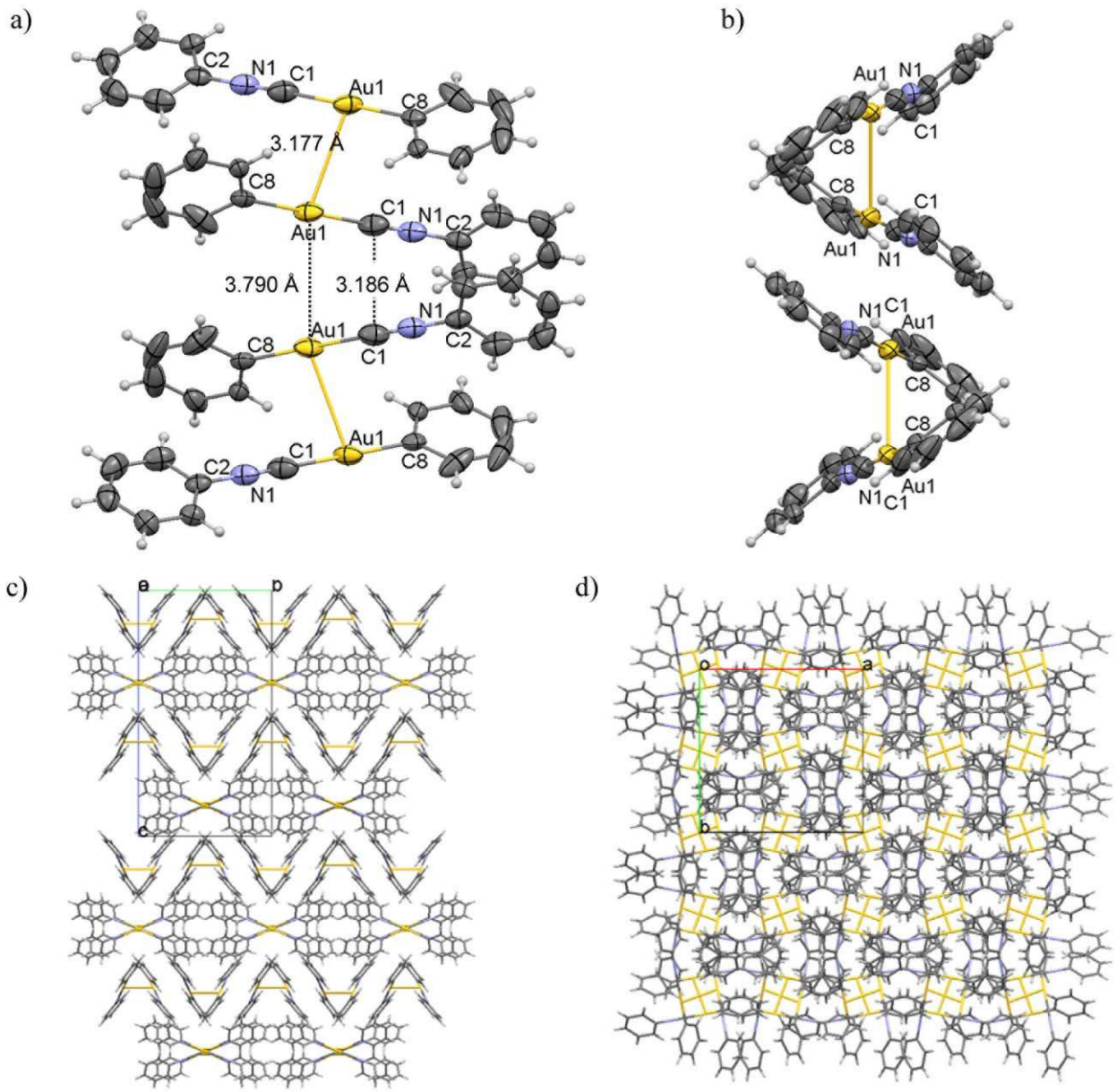

Supplementary Figure S9. X-ray crystallographic analysis of $\mathbf{II}_{\mathbf{y}}$ (CCDC 897541). a) ORTEP structure of the tetrameric structure of a 1D chain of **1**. b) Side view of a). c) Molecular packing viewed along the *a* axis. d) Molecular packing viewed along the *c* axis.

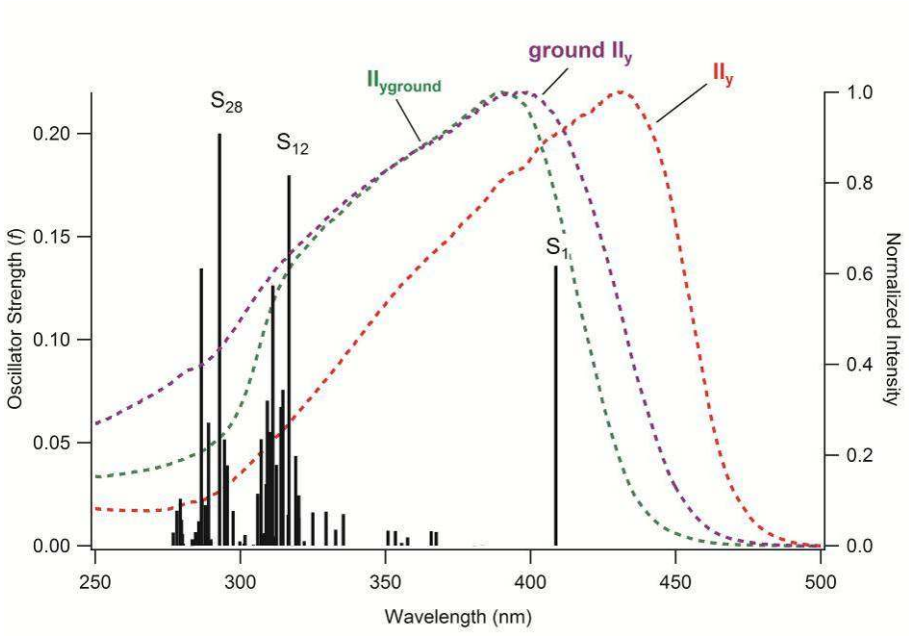

Supplementary Figure S10. Excitation spectra of ground **I$_b$** (**II$_{y(ground\ Ib)}$**, green), **II$_y$** (red), and a ground sample of **II$_y$** (purple). TD transitions calculated using B3LYP are overlaid.

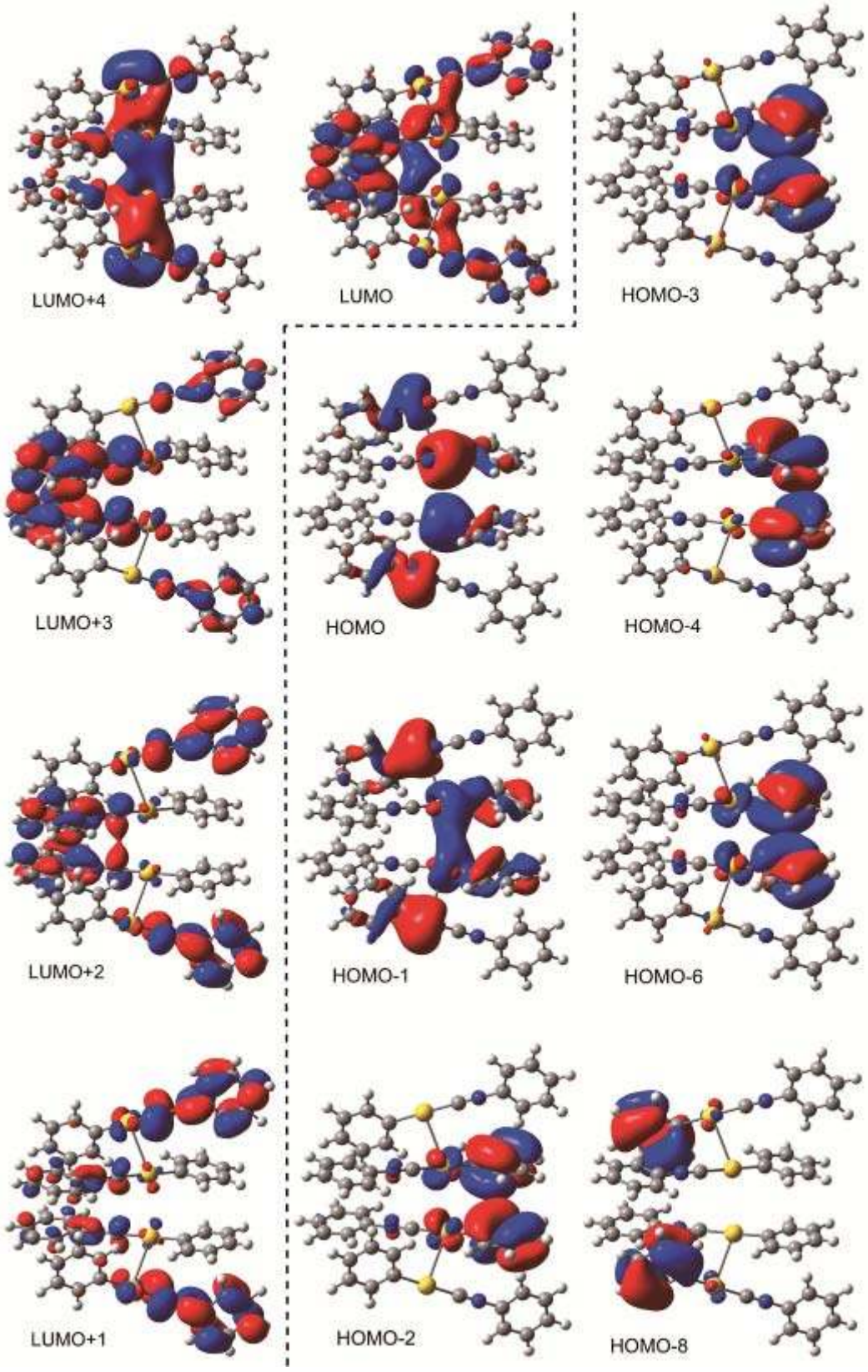

Supplementary Figure S11. Molecular orbitals of a model tetrameric structure of $\mathbf{II_y}$.

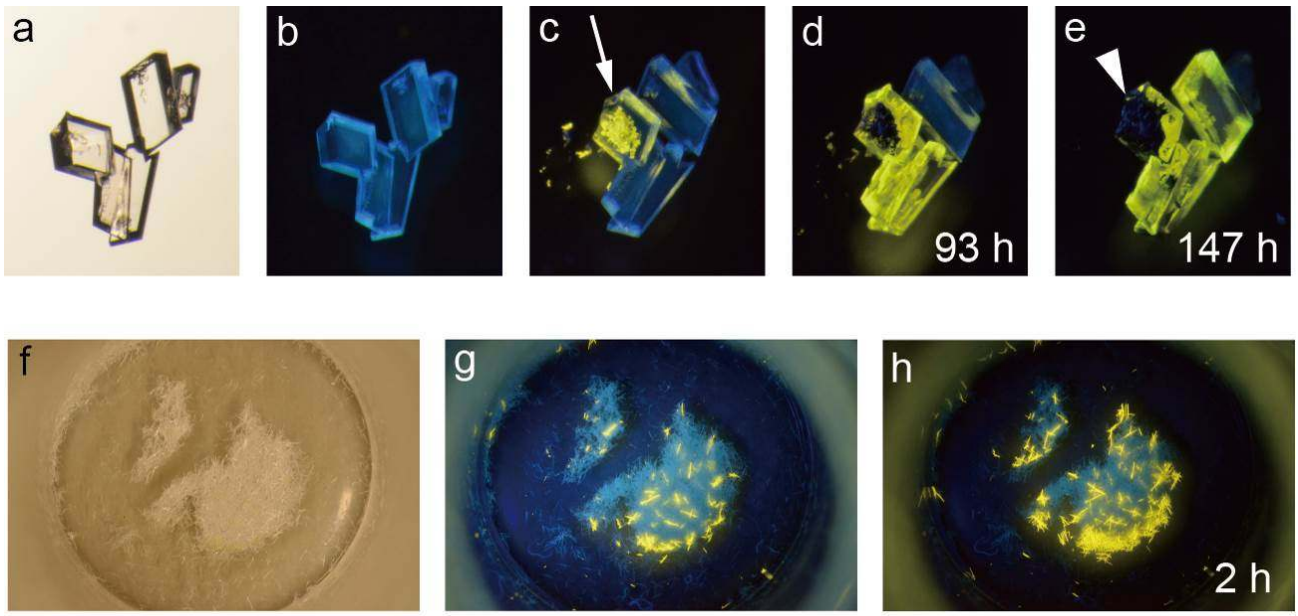

Supplementary Figure S12. Photographs of the phase transformation. $\mathbf{I_b}$ crystals under (**a**) ambient light and (**b**) UV light. (**c**) Mechanical stimulation-induced phase transformation (white arrow). Phase progression after (**d**) 93 h and (**e**) 147 h. A black precipitate of metallic gold was observed on the crystal surface around the initial contact area (e, white triangle). Photographs of the phase progression in a mixture of $\mathbf{I_b}$ and $\mathbf{II_y}$ under ambient light (**f**), UV light (**g**), and under UV light after 2 h (**h**).

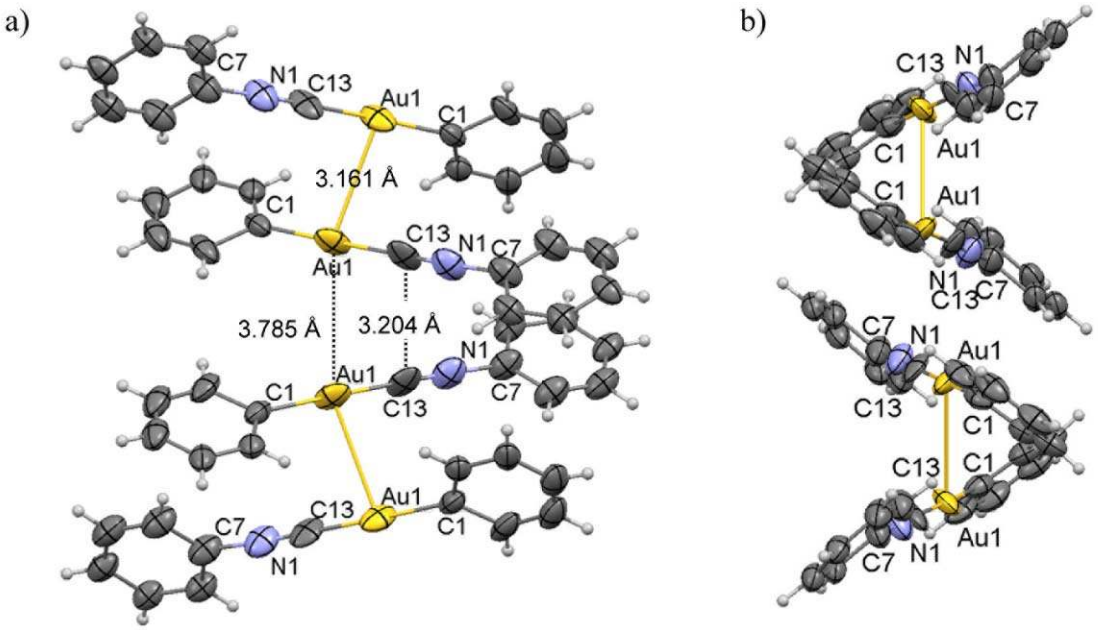

Supplementary Figure S13. X-ray crystallographic analysis of $\mathbf{II}_{\mathbf{yscsc}}$ (CCDC 897542). The single crystal sample was prepared by mechanical pricking-induced SCSC transformation. The pricked area was removed prior to data collection. a) ORTEP structure of the tetrameric structure of a 1D chain of **1**. b) Side view of a).

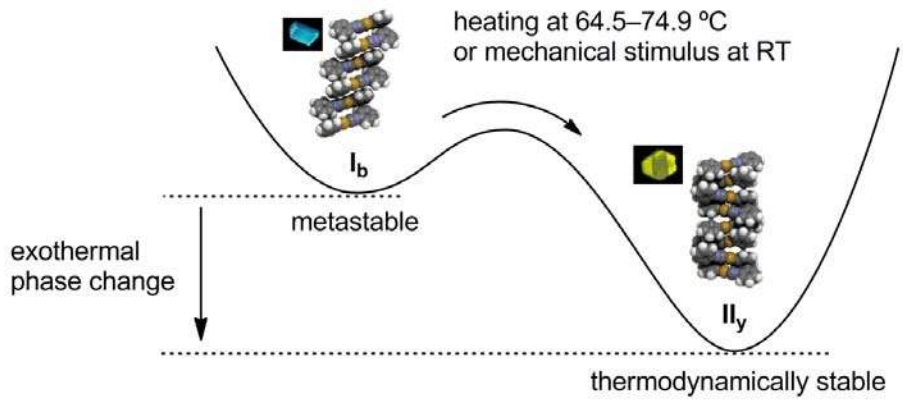

Supplementary Figure S14. Diagram of the thermodynamic energies for $\mathbf{I_b}$ and $\mathbf{II_y}$.

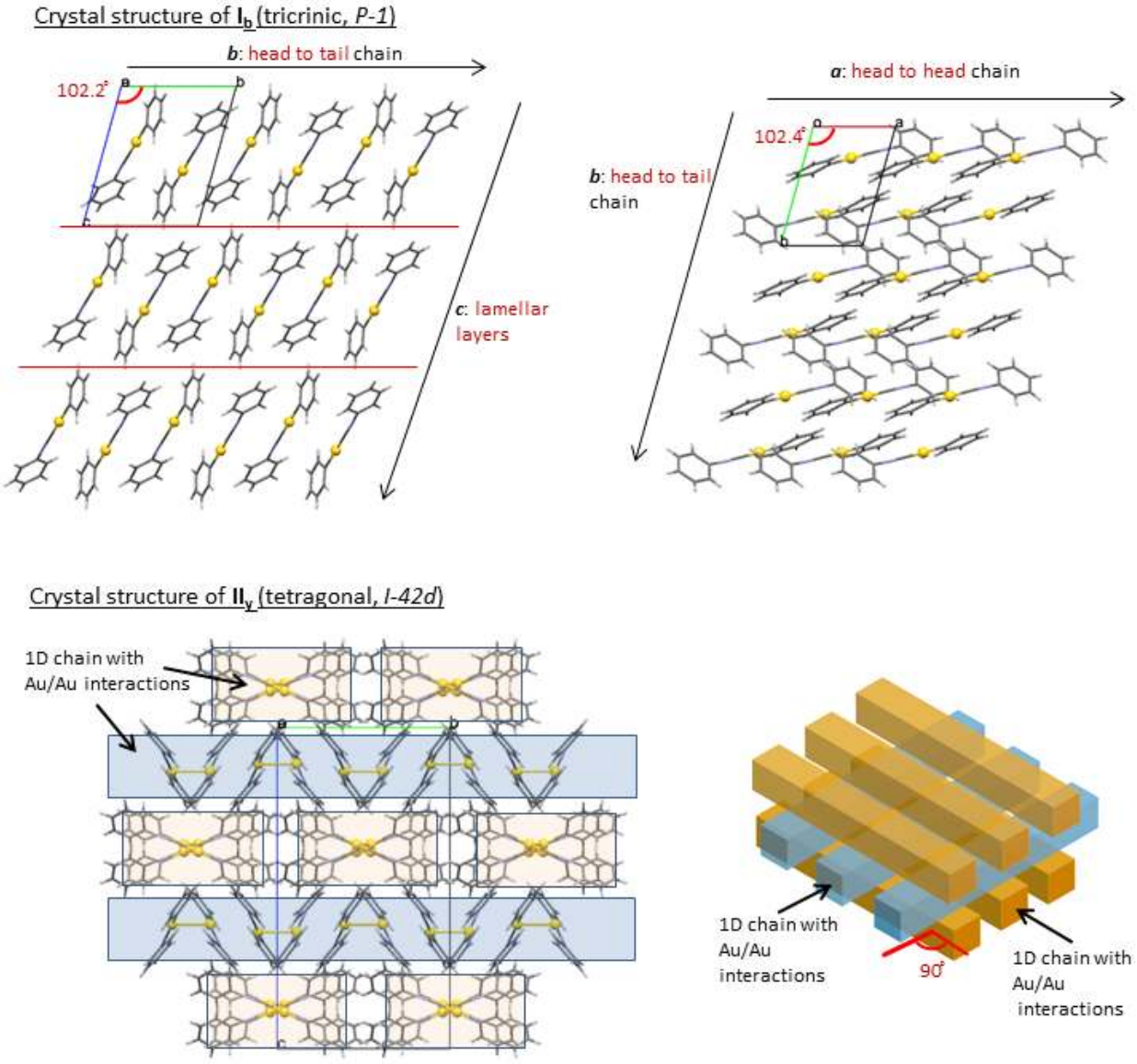

Supplementary Figure S15. Comparison of the structures of $\mathbf{I_b}$ and $\mathbf{II_y}$.

Supplementary Table S1. Summary of X-ray Crystallographic Data for $\mathbf{I_b}$, $\mathbf{II_y}$, and $\mathbf{II_{yscsc}}$.

Compound	$\mathbf{I_b}$	$\mathbf{II_y}$	$\mathbf{II_{yscsc}}$
	CCDC 909344	CCDC 897541	CCDC 897542
Empirical Formula	$C_{13}H_{10}AuN$	$C_{13}H_{10}AuN$	$C_{13}H_{10}AuN$
Formula Weight	377.20	377.20	377.20
Crystal System	triclinic	tetragonal	tetragonal
Crystal Size	0.320×0.210×0.020 mm	0.240×0.220×0.130 mm	0.400×0.200×0.100 mm
a	6.0214(5) Å	13.4781(4) Å	13.4075(19) Å
b	9.0729(8) Å		
c	11.4498(10) Å	24.8079(8) Å	24.9673(19) Å
α	102.159(7)°		
β	101.468(7)°		
γ	102.358(7)°		
V	577.51(9) $Å^3$	4506.6(2) $Å^3$	4488.1(1) $Å^3$
Space Group	*P-1* (#2)	*I-42d* (#122)	*I-42d* (#122)
Z value	2	16	16
D_{calc}	2.169 g/cm^3	2.224 g/cm^3	2.233 g/cm^3
Temperature	123 K	123 K	123 K
$2\theta_{max}$	54.9°	54.9°	55.0°
$\mu(MoK_\alpha)$	127.459 cm^{-1}	131.206 cm^{-1}	131.206 cm^{-1}
No. of Reflections Measured	Total: 5621	Total: 18053	Total: 17818
	Unique: 2632	Unique: 2100	Unique: 2581
	(R_{int} = 0.0348)	(R_{int} = 0.0811)	(R_{int} = 0.1010)
		Friedel pairs: 928	Friedel pairs: 1149
No. of Observations (All reflections)	2632	2100	2581
Residuals: R_1 (I>2.00σ(I))	0.0326	0.0252	0.0883
Residuals: wR_2 (All reflections)	0.0819	0.0536	0.2174
Goodness of Fit Indicator (GOF)	1.056	1.093	1.316
Maximum peak in Final Diff. Map	0.75 e^- /$Å^3$	0.72 e^- /$Å^3$	2.32 e^- /$Å^3$
Minimum peak in Final Diff. Map	–0.91 e^- /$Å^3$	–0.80 e^-/$Å^3$	–1.68 e^- /$Å^3$

Supplementary Table S2. Selected Bond Lengths (Å) and Angles (º) for $\mathbf{I_b}$, $\mathbf{II_y}$, $\mathbf{II_{yscsc}}$.

$\mathbf{I_b}$								
Bond Lengths	Au(1)	C(1)	1.977(8)		Au(1)	C(8)	2.022(6)	
	N(1)	C(1)	1.155(9)		N(1)	C(2)	1.402(8)	
Bond Angles	C(1)	Au(1)	C(8)	180.0(3)	Au(1)	C(1)	N(1)	176.9(6)
	C(1)	N(1)	C(2)	178.6(7)				
$\mathbf{II_y}$.								
Bond Lengths	Au(1)	C(1)	1.981(9)		Au(1)	C(8)		2.034(7)
	N(1)	C(1)	1.152(11)		N(1)	C(2)		1.396(10)
	Au(1)	Au(1)	3.1773(4)		Au(1)	Au(1')		3.790
Bond Angles	C(1)	Au(1)	C(8)	178.1(3)	Au(1)	C(1)	N(1)	179.5(8)
	C (1)	N (1)	C (2)	179.5 (8)				
$\mathbf{II_{yscsc}}$.								
Bond Lengths	Au(1)	C(13)	1.93(3)		Au(1)	C(1)		2.01(3)
	N(1)	C(13)	1.16(4)		N(1)	C(7)		1.48(4)
	Au(1)	Au(1)	3.161(2)		Au(1)	Au(1')		3.785
Bond Angles	C(1)	Au(1)	C(13)	178.8(11)	Au(1)	C(13)	N(1)	176(3)
	C(7)	N(1)	C(13)	177(3)				

Supplementary Table S3. Elemental Analysis of Crystals of **1**

Entry		C	H	N
	Calculated for **1** ($C_{13}H_{10}AuN$)	41.40	2.67	3.71
1	$\mathbf{I_b}$	41.68	2.90	3.68
2	$\mathbf{II_y}$ (crystallized from solution)	41.25	2.87	3.77
3	$\mathbf{II_{y(ground\ Ib)}}$ (ground $\mathbf{I_b}$)	41.51	2.80	3.72
4	$\mathbf{II_{yscsc}}$ (mechanical pricking of $\mathbf{I_b}$)	41.61	2.84	3.37
5	$\mathbf{II_{yscsc}}$ (solid seeding of $\mathbf{I_b}$)	41.23	2.93	3.69
6	$\mathbf{II_{yscsc}}$ (heating of $\mathbf{I_b}$, decompose)	40.96	2.58	3.42

Supplementary Table S4. Calculated Potential Energies.

Orbital	**1** in $CHCl_3$ (eV)	Tetramer in crystal $\mathbf{I_b}$ (eV)	Tetramer in crystal $\mathbf{II_y}$ (eV)
LUMO+6	0.368541605	–1.198076012	–0.73643795
LUMO+5	0.115563978	–1.259299083	–0.740337955
LUMO+4	0.057417826	–1.295185954	–0.951210061
LUMO+3	–0.162546607	–1.664973371	–1.408852418
LUMO+2	–0.931119421	–1.748609116	–1.555627184
LUMO+1	–1.22259051	–2.017121125	–1.682561205
LUMO	–1.97758642	–2.017375709	–1.880844298
HOMO	–6.303001356	–5.76668981	–5.484283716
HOMO-1	–6.552852444	–5.766861025	–5.862440382
HOMO-2	–6.64875298	–6.034408497	–6.122361395
HOMO-3	–7.401870991	–6.046453004	–6.238055485
HOMO-4	–7.696440697	–6.124690082	–6.241776862
HOMO-5	–8.23150734	–6.12493017	–6.270656778
HOMO-6	–8.276121003	–6.390020271	–6.298387221
HOMO-7	–8.333792751	–6.394333582	–6.326189014

Supplementary Table S5. TDDFT Calculations for **1**: Calculated Wavelength ($\lambda_{calculated}$), Energy Levels, Oscillator Strengths (*f*), and Orbital Transition Analysis.

states	$\lambda_{calculated}$ (nm)	energy (eV)	*f*	orbital transition analysis	
S_1	327.69	3.7836	0.0011	HOMO → LUMO (LLCT)	0.70137
S_2	312.69	3.9651	0.0127	HOMO–2 → LUMO (MLLCT)	0.70066
S_4	274.00	4.5250	0.4172	HOMO → LUMO+1	0.70046
S_8	250.05	4.9585	0.8412	HOMO–3 → LUMO (ππ*)	0.8412

Supplementary Table S6. TDDFT Calculations for $\mathbf{I_b}$: Calculated Wavelength ($\lambda_{calculated}$), Energy Levels, Oscillator Strengths (*f*), and Orbital Transition Analysis.

states	$\lambda_{calculated}$ (nm)	energy (eV)	*f*	related orbitals (analysis)	
S_2	387.12	3.2027	0.0242	HOMO–1 → LUMO (LLCT)	0.49546
				HOMO → LUMO+1 (LLCT)	0.49544
S_3	356.48	3.4780	0.0202	HOMO–3 → LUMO	–0.47753
				HOMO–2 → LUMO+1	0.49497
S_5	354.19	3.5005	0.0298	HOMO– → LUMO+3	–0.37881
				HOMO → LUMO+2	0.57903
S_{13}	333.31	3.7198	0.0317	HOMO–9 → LUMO	0.19157
				HOMO–8 → LUMO+1	0.19972
				HOMO–7 → LUMO+1	0.42694
				HOMO–6 → LUMO	0.43547
				HOMO–2 → LUMO+2	–0.18320
S_{17}	325.77	3.8059	0.0379	HOMO–5 → LUMO+3	–0.36122
				HOMO–4 → LUMO+2	0.52408
				HOMO–3 → LUMO	0.19219
				HOMO–2 → LUMO+1	0.19418
S_{28}	312.98	3.9614	0.0732	HOMO–1 → LUMO+4	0.56832
				HOMO–1 → LUMO+6	0.13628
				HOMO → LUMO+5	–0.32090
				HOMO → LUMO+7	–0.18887
S_{32}	303.95	4.0791	0.2057	HOMO–5 → LUMO+3	–0.13785
				HOMO–3 → LUMO+4	–0.12986
				HOMO–1 → LUMO+6	0.50099
				HOMO → LUMO+5	0.35992
				HOMO → LUMO+7	–0.22764

Supplementary Table S7. TDDFT Calculations for **II$_b$**: Calculated Wavelength ($\lambda_{calculated}$), Energy Levels, Oscillator Strengths (*f*), and Orbital Transition Analysis.

states	$\lambda_{calculated}$ (nm)	energy (eV)	*f*	related orbitals (analysis)	
S_1	408.65	3.0340	0.1358	HOMO–1 → LUMO+1 (MMLCT)	0.10423
				HOMO→ LUMO (MMLCT)	0.69354
S_{12}	316.71	3.9148	0.1858	HOMO–4 → LUMO (LLCT)	0.11174
				HOMO–8 → LUMO (LLCT)	–0.26059
				HOMO–1 → LUMO+1 (MMLCT)	0.1846
S_{28}	292.80	4.2345	0.2102	HOMO–6 → LUMO+1	0.25187
				HOMO–6 → LUMO+3	0.13053
				HOMO–4 → LUMO+1	–0.10938
				HOMO–3 → LUMO+2	0.44317
				HOMO–2 → LUMO+	0.15328
				HOMO–6 → LUMO+1	0.37865
				HOMO–1 → LUMO+3 (MMLCT)	–0.24008
				HOMO → LUMO+4 (MC)	0.51882
				HOMO–8 → LUMO (ππ*)	–0.26059
				HOMO–1 → LUMO+1 (MMLCT)	0.18467

Supplementary Note 1. Qualitative Analysis of Crystals.

Elemental Analysis: Values of the elemental analysis for $\mathbf{I_b}$, $\mathbf{II_y}$, $\mathbf{II_{y(ground\ Ib)}}$, and $\mathbf{II_{yscsc}}$ prepared by mechanical stimulation and crystal seeding methods (Table S2, entries 1–5) were consistent with the calculated values for **1**. A deviation in the percentage of carbon in the $\mathbf{II_y}$ prepared by heating $\mathbf{I_b}$ was observed (entry 6, Calcd: 41.40; Obs: 40.96), representing the partial chemical decomposition of **1**. This partial decomposition was also observed with a hot-stage microscope as a black precipitate of metallic gold. This demonstrates the high compound purity and the absence of any solvents in $\mathbf{I_b}$ and $\mathbf{II_y}$ crystals.

NMR analysis of $\mathbf{I_b}$ and $\mathbf{II_y}$: NMR measurements of $CDCl_3$ solutions of $\mathbf{I_b}$ and $\mathbf{II_y}$ crystals were conducted to confirm the sample purity and the absence of solvents (Figure S2). The crystals were completely dissolved in $CDCl_3$, and the NMR measurements were conducted using these solutions. Solvent levels higher than a 1% molar ratio are capable of being detected by the NMR measurement. However, no impurities and solvents were detected in these samples, indicating no solvent inclusion in either $\mathbf{I_b}$ or $\mathbf{II_y}$ crystals.

Single Crystal and Powder X-ray Analysis: The maximum peaks in the final differential maps for $\mathbf{I_b}$, $\mathbf{II_y}$, and $\mathbf{II_{yscsc}}$, (0.75 $e^-/Å^3$, 0.72 $e^-/Å^3$, 2.32 $e^-/Å^3$, respectively, Table S2) were below 0.075 Z_{max} $e^-/Å^3$ (for complex **1**, 5.925). This indicates that no residual electron density can be assigned to other molecules, such as solvent, present in the crystal.

TGA Analysis: The thermal gravimetric analysis (TGA) was performed under a nitrogen atmosphere under heating to 200 °C with a heating rate of 5 °C min^{-1} using a Bruker AXS TG-DTA 2010 (Figure S3b). The phase change from $\mathbf{I_b}$ to $\mathbf{II_y}$ was observed near 60–75 °C, although no significant mass loss or transition steps from $\mathbf{I_b}$ to $\mathbf{II_y}$ were observed. The partial decomposition of the complex began near 85 °C and was accompanied by mass loss. The mass loss ceased at 140 °C, with 52.3% of the original mass of the residue remaining. This residue corresponds to the Au composition of the complex (Au/ $C_{13}H_{10}AuN$ = 52.2%).

Supplementary Note 2. Thermal Analysis Using Differential Scanning Calorimetry (DSC) and Thermal Gravimetric Analysis (TGA).

The mechanical- or solid seeding-triggered phase change occurred at room temperature, but a thermal phase transformation was also observed at elevated temperatures using differential scanning calorimetry (DSC) analysis. Multiple exothermic peaks for the transition from $\mathbf{I_b}$ to $\mathbf{II_y}$ were observed at 64.5–74.9 °C upon heating at a rate of 10 °C/min, with a corresponding change in emission color from blue to yellow (Figure S3a). An endothermic peak was also recorded at 100.5 °C and was accompanied by the partial decomposition of the sample surface. The sample melted at 125.5 °C, corresponding to the melting point of $\mathbf{II_y}$; at this temperature, he color of the sample also changed from pale yellow to black. No reverse phase change was observed when the sample was cooled. The thermal analysis suggested that $\mathbf{I_b}$ was a metastable, kinetically isolated form of **1** (Figure S15). This phase can transition to the thermodynamically favored form $\mathbf{II_y}$ by heating at 64.5–74.9 ºC or by mechanical triggering at room temperature. The small exothermic peaks observed near 64.5–74.9 ºC correspond to the energy release accompanying the phase change, as shown in Figure S13a.[2] The use of mechanical pricking to trigger the thermal phase transformation has also been reported. In this case, the phase change occurred near the temperature of the thermal phase change.[1–3] However, the phase transformation of $\mathbf{I_b}$ occurred at a much lower temperature than the thermal phase change, suggesting that this transformation was triggered purely by mechanical stimulation. To our knowledge, this is the first clear example of solid seeding-triggered SCSC transformation. In addition, the emergence of metallophilic interactions after the SCSC transformation of mother crystals lacking metallophilic interactions has not been reported previously.

Supplementary Note 3. DFT Calculations.

General Calculation Methods: All calculations were performed using the Gaussian 09W (revision C.01) program package.[29] In the DFT and TDDFT calculations, SDD with 19 valence electrons was used for gold atom and cc-pVDZ was used for all other atoms, where B3LYP functionals were employed.[30–32] Molecular orbitals were drawn by the GaussView 5.0 program. The fully optimized geometry for monomeric PhAu(CNPh) (**1**) in $CHCl_3$ was calculated using Tomasi's polarizable continuum model (PCM).[33] The geometry for the TDDFT calculation of the tetrameric structures of **1** in $\mathbf{I_b}$ and $\mathbf{II_y}$ were optimized using redundant coordinates of C, N, and Au, which were taken from the corresponding X-ray structures, in which the positions of the heavy atoms were fixed and H atoms were equilibrated.[34–37] The results are summarized in Tables S4–7 and Figures S4–11.

TDDFT calculation of monomeric 1 in $CHCl_3$: We tested various calculation methods, including CAM-B3LYP, M062X, and LC-BLYP; however, only B3LYP provided acceptable values for the excitation (Figure S5). We therefore employed the B3LYP method for the TDDFT calculations of **1** in the solution and solid states ($\mathbf{I_b}$ and $\mathbf{II_y}$). The calculation results indicated that the lowest energy transition in solution corresponds to the highest occupied molecular orbital (HOMO)/lowest unoccupied molecular orbital (LUMO) transition, which arises due to ligand (phenyl on the gold atom) to ligand (isocyanide) charge transfer (LLCT, Figure S4, S6 and Table S5).

TDDFT calculation of the tetrameric model compound of $\mathbf{I_b}$: The coordinates of the model structure were generated by the partial optimization of the hydrogen atoms because the accuracy of the position of hydrogen in single X-ray analysis is not reliable. The TDDFT calculations were conducted using this modified atom coordinate. The low-lying singlet excited states were computed from the π orbital of the phenyl ligand to the π^* orbital of the isocyanide ligand (Figures S4, S7 and S8; Table S6). The calculated values for these LLCT transitions (325.77, 354.2, 356.48, and 387.12 nm) were consistent with the observed excitation peaks from 320 to 380 nm, with an edge at 400 nm (main text, Figure 1b, blue dotted line).

TDDFT calculation of the model tetrameric structure of $\mathbf{II_y}$: The low energy excitation peak (432 nm) observed for $\mathbf{II_y}$ crystals corresponds to the highest occupied molecular orbital (HOMO)/lowest unoccupied molecular orbital (LUMO) transition mixed with the HOMO-1/LUMO+1 transition (408.65 nm) and can be attributed to the σ^* (gold d_z) to isocyanide π^* transition (metal–metal to ligand charge transfer, Figures S10, S11; Table S7). However, it is difficult to fully explain the emission mechanism using this TDDFT approach based on ground state structures. The aurophilic interactions in $\mathbf{II_y}$ crystals should increase the emission wavelength by destabilizing the occupied d_z orbitals of the gold atoms (Figures S4 and 11; Table S4). In addition, the crystal structure of $\mathbf{II_y}$ allows the gold d_z orbitals to contribute more to the excited states than in $\mathbf{I_b}$, facilitating intersystem crossing from singlet to triplet excited states and phosphorescence from the lowest triplet excited state to the singlet ground state. The observation of a shorter emission lifetime and increased emission quantum yield compared to $\mathbf{I_b}$ is consistent with increased intersystem crossing.[38]

Supplementary Methods

1. Materials and Methods

Materials were obtained from commercial suppliers and purified by standard procedures unless otherwise noted. Solvents for synthesis were purchased from commercial suppliers, degassed *via* three freeze-pump-thaw cycles, and further dried over molecular sieves (4A). Solvents for recrystallization were purchased from commercial suppliers and used as received. NMR spectra were recorded on a JEOL JNM-ECX400P (Japan) spectrometer (^{1}H: 400 MHz and ^{13}C: 99.5 MHz). Tetramethylsilane (^{1}H) and $CDCl_3$ (^{31}C) were used as external standards. Mesitylene or 1,1,2,2-tetrachloroethane were used as an internal standard to determine the NMR yield. Absorption and emission spectra were recorded on Hitachi U-3300 and F-7000 spectrometers, respectively. The emission quantum yields (Φ^{em}) of the solid samples were recorded on an F-7000 spectrometer with an integrating sphere. Emission lifetime measurements were conducted using a streak camera (Hamamatsu Photonics, C4334) as a photo detector under excitation at 355 nm (Continuum Surelite-II, 355 nm, 6 ns pulse width). For the emission and absorption spectroscopy of a solution of the gold(I) complex, the sample solution was degassed by purging with a stream of nitrogen or argon gas for at least 30 min. Elemental analyses and low- and high-resolution mass spectra were recorded at the Center for Instrumental Analysis, Hokkaido University. Photographs were captured using Olympus BX51 and SZX7 microscopes with Olympus DP72, Nikon D5100 and RICOH CX1 digital cameras.

2. ^{1}H and ^{13}C NMR Data for Phenyl(phenyl isocyanide)gold(I) (1).

^{1}H NMR (400 MHz, $CDCl_3$): δ = 7.51–7.57 (m, 1H), 7.42–7.50 (m, 6H), 7.18 (t, J = 7.2 Hz, 2H), 7.04–7.10 (m, 1H); ^{13}C NMR (100 MHz, $CDCl_3$): δ = 162.6, 160 (m), 140.3, 131.1, 129.9, 127.4, 126.6, 126.1, 125 (m); HRMS (FAB^{+}): 377.0476 [(M)$^{+}$, 377.0479 ($C_{13}H_{10}AuN$)].

Supplementary References

27. CrystalStructure 4.0: Crystal Structure Analysis Package, Rigaku Corporation (2000-2010). Tokyo 196-8666, Japan.
28. G. M. Sheldrick, *Acta Crystallogr. A* **64**, 112 (2008).
29. Gaussian 09, Revision C.01, M. J. Frisch, G. W. Trucks, H. B. Schlegel, G. E. Scuseria, M. A. Robb, J. R. Cheeseman, G. Scalmani, V. Barone, B. Mennucci, G. A. Petersson, H. Nakatsuji, M. Caricato, X. Li, H. P. Hratchian, A. F. Izmaylov, J. Bloino, G. Zheng, J. L. Sonnenberg, M. Hada, M. Ehara, K. Toyota, R. Fukuda, J. Hasegawa, M. Ishida, T. Nakajima, Y. Honda, O. Kitao, H. Nakai, T. Vreven, J. A. Montgomery, Jr., J. E. Peralta, F. Ogliaro, M. Bearpark, J. J. Heyd, E. Brothers, K. N. Kudin, V. N. Staroverov, R. Kobayashi, J. Normand, K. Raghavachari, A. Rendell, J. C. Burant, S. S. Iyengar, J. Tomasi, M. Cossi, N. Rega, J. M. Millam, M. Klene, J. E. Knox, J. B. Cross, V. Bakken, C. Adamo, J. Jaramillo, R. Gomperts, R. E. Stratmann, O. Yazyev, A. J. Austin, R. Cammi, C. Pomelli, J. W. Ochterski, R. L. Martin, K. Morokuma, V. G. Zakrzewski, G. A. Voth, P. Salvador, J. J. Dannenberg, S. Dapprich, A. D. Daniels, Ö. Farkas, J. B. Foresman, J. V. Ortiz, J. Cioslowski, and D. J. Fox, Gaussian, Inc., Wallingford CT, 2009.
30. A. D. Becke, *Phys. Rev. A* **38**, 3098 (1988).
31. C. Lee, W. Yang, R. G. Parr, **37**, 785 (1988).
32. A. D. Becke, *J. Chem. Phys.* **98**, 5648 (1993).
33. J. Tomasi, B. Mennucci, R. Cammi, *Chem. Rev.* **105**, 2999 (2005).
34. R. Bauernschmitt, R. Ahlrichs, *Chem. Phys. Lett.* **256**, 454 (1996).
35. M. E. Casida, C. Jamorski, K. C. Casida, D. R. Salahub, *J. Chem. Phys.* **108**, 4439 (1998).
36. R. E. Stratmann, G. E. Scuseria, M. J. Frisch, *J. Chem. Phys.* **109**, 8218 (1998).
37. G. Scalmani *et al.*, *J. Chem. Phys.* **124**, 094107 (2006).
38. Rodríguez, L., Ferrer, M., Crehuet, R., Anglada, J. & Lima, J. C. *Inorg. Chem.* **51**, 7636 (2012).